RESEARCH ARTICLE | APRIL 01 2022

Investigations into the ventilated cavities around a surface-piercing hydrofoil at high Froude numbers

Renfang Huang (黄仁芳); Rundi Qiu (丘润荻); Yuchang Zhi (支玉昌); ... et. al

Physics of Fluids 34, 043304 (2022)
https://doi.org/10.1063/5.0085553

Physics of Fluids ARTICLE scitation.org/journal/phf

Investigations into the ventilated cavities around a surface-piercing hydrofoil at high Froude numbers

Cite as: Phys. Fluids **34**, 043304 (2022); doi: 10.1063/5.0085553
Submitted: 18 January 2022 · Accepted: 9 March 2022 ·
Published Online: 1 April 2022

View Online Export Citation CrossMark

Renfang Huang (黄仁芳),[1] Rundi Qiu (丘润荻),[1,2] Yuchang Zhi (支玉昌),[3] and Yiwei Wang (王一伟)[1,2,4,a)]

AFFILIATIONS

[1]Key Laboratory for Mechanics in Fluid Solid Coupling Systems, Institute of Mechanics, Chinese Academy of Sciences, Beijing 100190, China
[2]School of Future Technology, University of Chinese Academy of Sciences, Beijing 100049, China
[3]School of Aeronautics and Astronautics, Sun Yat-Sen University, Guangzhou 510275, China
[4]School of Engineering Science, University of Chinese Academy of Sciences, Beijing 100049, China

[a)]Author to whom correspondence should be addressed: wangyw@imech.ac.cn

ABSTRACT

This study investigates the ventilated cavities around a surface-piercing hydrofoil, aiming to extend previous studies by an in-depth understanding of the vaporous cavity behaviors and the flow-regime transition at high Froude numbers. An experiment is carried out in a constrained-launching water tank with a vertically cantilevered hydrofoil piercing a still water surface. The cavity is recorded using high-speed photography, and flow-regime maps are summarized over a broad range of Froude number and yaw angle at different immersed aspect ratios. In addition to the well-known steady flow regimes (i.e., fully wetted flow and fully ventilated flow), an unsteady vaporous cavitating flow is revealed at a very high Froude number with a small yaw angle, which exhibits cavitation shedding dynamics behaviors, including the cavity growth, destabilization, and collapse. The transition from the fully wetted flow to the fully ventilated flow is attributed to the vapor-cavitation-induced ventilation besides the tip-vortex-induced ventilation. Vaporous cavitation promotes ventilation formation, but it has to meet the criterion that air should enter the sub-atmospheric cavity through the tip-vortex path before the cavity length reaches the maximum. Moreover, an improved lifting-line model is developed with considering the effects of free surface and finite aspect ratio. Both analytical modeling and experimental measurements reveal that the vaporous cavity length follows a power relation against the cavitation parameter. Such knowledge lays a foundation for the design optimization and control strategy of high-speed hydrofoils.

I. INTRODUCTION

Atmospheric ventilation is a special case of ventilation that the noncondensable gas would enter the liquid water, create a ventilated cavity, and encompass a surface-piercing body. In this case, the ventilated gas is supplied from the free surface rather than by artificial pumping or blowing. The ventilated cavity helps to reduce the skin friction drag and improve the stability of the lift-generating body, and thus, it is of great interest for marine engineering. Examples include hydrofoils, surface-piercing propellers, and high-speed crafts with struts or rudders. This process generally depends on the physical parameters: the forward velocity (u), the immersed depth of the hydrofoil tip (h), and the yaw angle (α). The first two parameters are, respectively, nondimensionalized as Froude number (Fr) and the immersed aspect ratio (AR).

In the published literature, three primary flow regimes have been widely observed: fully wetted (FW) flow, partially ventilated (PV) flow, and fully ventilated (FV) flow. In FW flows, two lateral sides of the hydrofoil are entirely wrapped by the liquid water, a white-water (foamy, aerated) wake flow appears at the blunt trailing edge, which will not affect the hydrodynamic performance of the hydrofoil.[1] The shape of the water surface is closely dependent on the forward velocity, and it is deformed deeper with the increase in the velocity.[2] Partially ventilated (PV) flows usually occur at low-to-moderate Froude numbers ($0.5 < Fr_h < 2$) across a wide range of angles of attack.[3–5] In this case, the cavity neither occupies the entire submerged span of the hydrofoil nor meets the stability criterion, that is the angle of the cavity-closure line exceeds 45°.[4] The fully ventilated (FV) flow is defined as the case where the suction side of the hydrofoil is covered by a stable cavity along the entire submerged span, and the pressure side of the hydrofoil is completely wet.[5] At high speeds, only FW and FV flows are present in the flow-regime map, and the partial ventilation disappears.[6] To date, ventilated cavities around surface-piercing bodies have been studied by a large number of scholars,[1–11] such as Kiceniuk,[9] Wetzel,[12] Wadlin,[13] Breslin and Skalak,[3] and Harwood *et al.*[4]

Kiceniuk[9] performed experiments on vertically surface-piercing hydrofoils at three different aspect ratios ($AR = 0.975$, 1.36, and 1.96). They found that gas ventilation occurred spontaneously when the yaw angle exceeded the stall angle, causing a great loss in the lift; such established cavity could remain stable even at sub-stalled angles, which was also observed by Wetzel[12] and Breslin and Skalak.[3] Wetzel[12] further reported that ventilation at high-α was correlated with Fr based on the experimental data for vertically streamlined struts.

Wadlin[13] conducted experiments for a surface-piercing hydrofoil having a NACA66 section by using the oil-flow technique, and a laminar separation bubble was visualized via the accumulated oil. They found that when the air was artificially introduced into the separation area, the air would occupy this area and induce a sealed cavity, but the ventilated cavity gradually dissipated once the disturbance was removed. Therefore, Wadlin[13] concluded that low pressures and boundary layer separations were required for the ventilation occurrence and air paths must remain available to maintain ventilation. Three air ingestion paths have been observed: at the nose, at the trailing edge, and through the tip-vortex.[7]

Harwood *et al.*[4] investigated atmospheric ventilation of a surface-piercing hydrofoil with an emphasis on the ventilation transition and stability. The test Froude number was $Fr_h = 0.5$–5, the aspect ratio was $AR = 0.5$–1.5, and the yaw angle was $\alpha = -5°$–$30°$. In this series of experiments, due to the hysteresis effect, the FW region overlapped the PV and FV regions, forming bi-stable regions. They proposed a stability criterion on the cavity topology, that is, the angle of the reentrant jet was not more than 45°.

Young *et al.*[6] made a comprehensive summary of the ventilation physics and its scaling effects, and they divided the ventilation formation mechanisms into several categories, including stall-induced ventilation,[3,4,9,12] tail ventilation,[2,7,8] tip-vortex-induced ventilation,[3,4,7,14] and perturbation-induced ventilation.[3–5,8,13,15] The first three cases are collectively referred to as the "spontaneous formation" mechanisms, in which sufficient vortex is generated by inherent features of the flow. In the fourth case, air may be artificially introduced into the separated flow[4,7,8,13] or by the free-surface disturbances, such as waves.[7,15]

Although most existing studies are limited to low-to-moderate Froude numbers, vaporous cavitation would inevitably occur when either the velocity is very high or the local pressure is below the saturated vapor pressure.[16] Vaporous cavitation can provide a ventilation-ready region filled with separated and sub-atmospheric flows,[17,18] and it is regarded as a secondary factor that may enhance or alter the above-mentioned ventilation mechanisms, leading to cavitation-induced ventilation.[7]

However, only a few scholars have observed such vaporous cavities and cavitation-induced ventilation for surface-piercing bodies.[2,5,7,8,19] Coffee and McKann[19] first observed this phenomenon on a vertically surface-piercing hydrofoil when the speed exceeded 23 m/s ($Fr_h > 16$), but there was no ventilation. Waid conducted a series of experiments for vertical surface-piercing struts in a depressurized towing tank, and the minimum cavitation number was 0.16.[2] In Waid's experiments, the attached cavity was disrupted by the reentrant jet from the rear and sides of the cavity, resulting in periodic shedding of the cavity and large force fluctuations, and the vapor cavitation number was the dominant parameter affecting the ventilation inception. Waid[2] suggested that Taylor instabilities[20] from initial small disturbances on the water surface were the most probable trigger of air penetration into the vaporous cavity, and the initial disturbances may be generated by the shed vorticity from the strut boundary layer.

A family of five symmetric struts were conducted a series of experiments by Rothblum *et al.*[8] in a high-speed towing tank to study the effects of speeds ($Fr_h = 0.69$–16.35), aspect ratios ($AR = 1$–3), and geometric parameters on the ventilation, cavitation, and other hydrodynamic characteristics. Patches of vaporous cavitation first appeared at the strut leading edge. With a gradual increase in the speed and/or yaw angle, the vaporous cavity spread vertically downward to the strut tip and upward nearly to the free surface until it completely covered the strut side. However, a thin layer of water was present between the cavity and the free surface and it was eventually breached, permitting air rapidly to enter the ventilation-prone vaporous cavity. Rothblum *et al.*[8] also speculated that ventilation inception may be attributed to Taylor instabilities on the thin layer of water promoted by a dramatic downward acceleration.

Rothblum[5] further studied a NACA0012-Mk-II strut in a high-speed channel with a free surface. The strut with a 102 mm chord was vertically piercing the free surface at $AR = 2.5$ and $Fr_h = 2.85$–12.04. The mode of ventilation inception was observed to change from tail ventilation at low speeds to nose ventilation at moderate speeds and then back to tail ventilation at the highest speeds. Moreover, Rothblum[5] revealed an interesting ventilation mode at intermediate speeds, where the aerated and separated water in the tail would interact with an oscillating vaporous cavity at the nose and the inception point of the ventilation was about the midspan.

Swales *et al.*[7] conducted experiments for the blunt-nosed biogive at atmospheric pressure and reduced pressure of 4667 Pa. The test velocity range was 1.5–6.1 m/s and the aspect ratio was $AR = 2$. They found that the decrease in the ambient pressure reduced the ventilation inception angle, but it slightly affected the washout angles. At atmospheric pressure, neither the ventilation inception angle nor the washout angle was not much affected, and the discontinuity of the ventilation inception angles was caused by the change in the ventilation mode from tail to nose, as demonstrated by Rothblum.[5]

Apart from the experimental research, a high-fidelity large eddy simulation was used to study the air-entraining flow around a surface-piercing hydrofoil with emphases on the wave patterns, free surface elevation, and frequency spectra.[21] Moreover, Hu *et al.*[22] quantitatively analyzed the flow structures of the breaking wave and found three bubble formation mechanisms during the air entrainment process. Bubble dynamics in the cavitating flow, like the bubble size oscillations, were captured by using a multi-scale Eulerian–Lagrangian approach with the micro-scale bubbles tracking by the Rayleigh–Plesset equation and a bubble motion equation.[23] As for the ventilation elimination during the deceleration process of a surface-piercing hydrofoil, Zhi *et al.*[24] numerically confirmed the importance of the re-entrant jet on the ventilation stability, which was proposed by Harwood *et al.*[4] Wang *et al.*[25] numerically studied the ventilation mechanism of a high-speed surface-piercing hydrofoil, and their results indicated that the natural supercavity would transit to the FV state through the cavitation-induced ventilation and the ventilation position was affected by the Taylor instability.

In addition to the cavitation-induced ventilation mentioned above, including the vaporous cavity shedding and the Taylor instabilities, Young *et al.*[6] also indicated that vaporous cavitation might increase the possibility of the tip-vortex ventilation, since the larger buoyancy of a cavitating vortex core would cause it to disrupt the free surface earlier than a sub-cavitating vortex. However, there are few reports about the cavitation promotion on the tip-vortex ventilation inception, and their interaction mechanism is also not clear. Hence, in this paper, we have attempted to conduct an experimental investigation for a surface-piercing hydrofoil in a constrained-launching tank under atmospheric pressure, and the purpose is to give an in-depth understanding of ventilated cavities at low-to-high Froude numbers, including flow regimes, ventilation formation mechanisms, and flow-regime stability boundaries.

The present paper is structured as follows. Section II is the experimental approach including the facility, experiment setup, and measurements together with data processing. In Sec. III, we first introduce the flow regimes and the ventilation formation observed in experiments. Subsequently, these flow regimes and unsteady transitions under different conditions are summarized in a flow-regime map, and the cavitation stability boundaries are quantitatively analyzed by using an improved lifting-line model. Finally, the conclusion and discussion are provided in Sec. IV.

II. EXPERIMENTAL APPROACH

Our experiments expand upon previous studies and contribute to comprehensive insights into the ventilated cavities of a surface-piercing hydrofoil at low-to-high Froude numbers.

A. Experimental platform and plate hydrofoil

Experiments are conducted in a constrained-launching water tank at the Institute of Mechanics, Chinese Academy of Sciences, as shown in Fig. 1, which is composed of a carriage, a sliding track, a buffer device, a displacement hydraulic system, a rubber band, and a steel frame. The test section is 2.95 m long with a $1.0 \times 1.0\,\mathrm{m}^2$ cross section.

The plate hydrofoil used in our experiments has the same section along the spanwise direction, as shown in Fig. 2. The section is an isosceles triangle, with a 50 mm chord and a vertex angle of 20°. The hydrofoil has a rectangular planform, and the span is 250 mm. It is made of 1045 steel as a whole. A metal disk is welded to the root of the plate hydrofoil, whose diameter is 120 mm and thickness is 5 mm. Screw holes are punched at the disk around two circles with a radius of 40 and 50 mm, respectively. The angular spacing between the screw holes is 10°.

The blockage ratio (B) is used to quantify the effects of the facility size on the test results, which is defined as the relative width of the foil triangular section over the facility width. Based on the experiments by Karn *et al.*,[26] $B = 5\%$ is proved to have little effect on the supercavities at high Froude numbers. In our experiment, the maximum blockage ratio is $B_{\max} = 1.71\%$, which is less than 5%, so the size of the constrained-launching tank is adequate to conduct the experiments for a surface-piercing hydrofoil.

B. Experimental setup

First, the rubber band is hung on the drawbar and the metal rod is inserted into the sleeve of the carriage [Fig. 3(a)], so the connection between the rubber band and the carriage is achieved. Subsequently, the displacement hydraulic system is used to pull back the carriage together with the rubber band along the sliding track. In the meanwhile, the rubber band is elastically deformed and generates an elastic force. Once the rod is pulled out from the sleeve, the fixed connection between the carriage and the rubber band is released, and the carriage is immediately ejected via the elastic force of the rubber band. The forward velocity u can be varied by changing the amount of elastic deformation of the rubber band. Afterward, the carriage moves forward along the sliding track. The total sliding distance is about 5 m. Finally, the sliding process would stop once the carriage hits the buffer device.

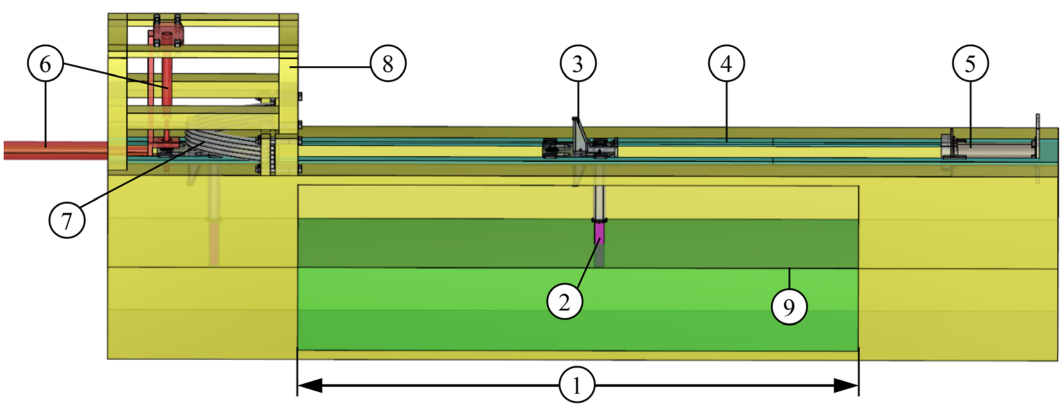

1. Test section: 2.95m × 1.0m × 1.0m, 2. Plate hydrofoil, 3. Carriage, 4. Sliding track, 5. Buffer device, 6. Displacement hydraulic system, 7. Rubber band, 8. Steel frame, 9. Calm water surface

FIG. 1. Schematic of the constrained-launching tank facility at Institute of Mechanics, Chinese Academy of Sciences.

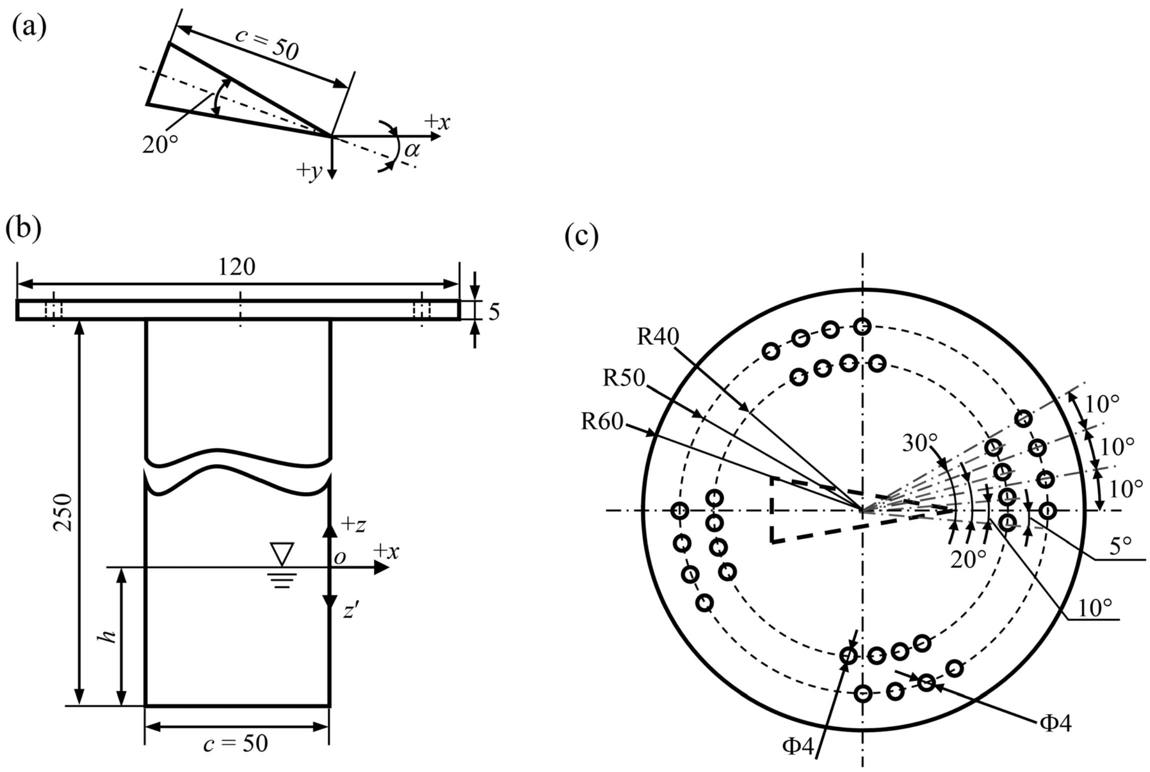

FIG. 2. (a) Cross section of the plate hydrofoil that was made of 1045 steel. (b) Foil geometrical dimensions and the coordinate system. (c) Top view. The yaw angle was adjusted through the pre-designed screw holes. Angular spacing between screw holes was 10°. The dimensions in the figure are in millimeters.

The plate hydrofoil is assembled on a strut, which is fastened to the carriage as shown in Fig. 3(a), and the yaw angle (or angle of attack, α) can be precisely adjusted through the screw joint of the metal disk. The plate hydrofoil is slung vertically to pierce the free surface. The immersed depth h is varied by adding or draining water and then sighting the waterline at tick marks along the hydrofoil span. The water temperature is the same as the room temperature (25 °C), and all experiments are carried out under a standard atmospheric pressure (1.01×10^5 Pa).

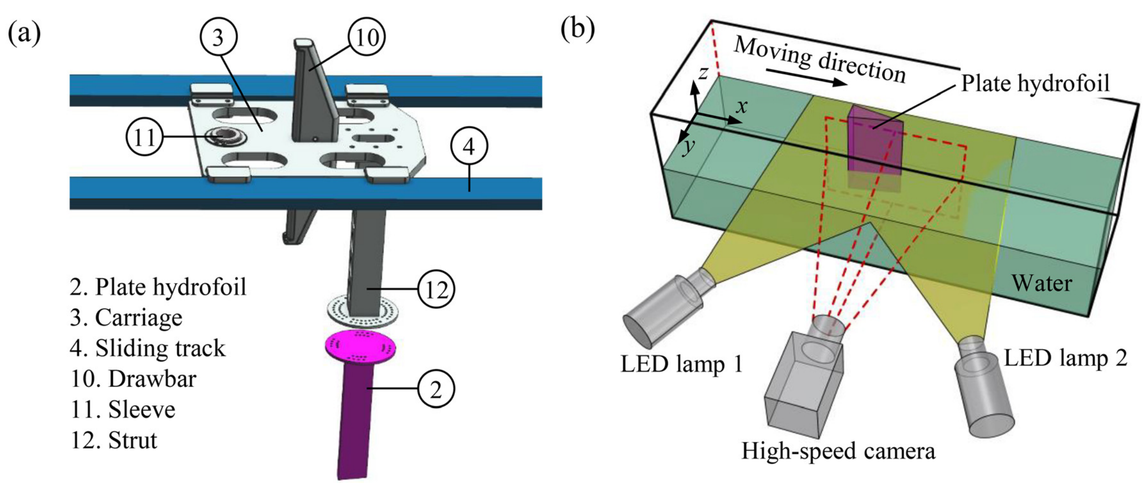

FIG. 3. Experimental setup. (a) The assembly diagram for the surface-piercing hydrofoil. (b) Images were captured by one high-speed camera from the front view. Illumination was provided by two LED lamps from oblique viewing angles.

C. Videography of the surface-piercing flow

The front side of the test section is made of Plexiglas, which allows us to observe the surface-piercing process. A large black cloth is attached to the rear side of the test section to absorb the reflected light. As shown in Fig. 3(b), a certain fixed area is illuminated where the hydrofoil passes by two 480W LED lamps (FALCONEYES® CLL-4800TDX) from the oblique viewing angles. An ultrahigh-speed camera (Phantom® v1612) is placed outside the test section to record both cavities below the free surface and spray sheets above the free surface. The center point of the camera is flush with the free surface. The camera is outfitted with a Canon lens (EF 24–70 mm f/2.8L II USM). High-speed images are recorded with a spatial resolution of 1280 × 800 at 10 000–20 000 frames per second. The lower frame rate is used for experimental conditions with slower velocities, and vice versa.

D. Experimental procedure and data processing

Experiments for the plate hydrofoil are performed with three immersed depths ($h = 0.025$, 0.05 and 0.075 m), five yaw angles ($\alpha = 0°$, $5°$, $10°$, $15°$, and $20°$), and various velocities. The corresponding aspect ratio is $AR = 0.5$–1.5, and the chord Froude numbers are over a low-to-high range of $Fr_h = 0.51$–43.34. Foil geometrical dimensions and the ranges of experimental conditions are listed in Table I. The experiments are carried out by changing u for each combination of α and h, then changing α for each fixed h, and finally changing h when all values of u and α have been tested. Even if the present amount of elastic deformation of the rubber band is the same as the last trial, we still cannot guarantee the same velocity due to the instabilities of the constrained-launching system. Therefore, to ensure the objectivity and repeatability of the experimental results, each trial is repeated at least five times until three very similar results are obtained, and the corresponding Froude number is provided for each case presented below.

A MATLAB code is developed to automatically track the hydrofoil position and calculate the velocity by using a rectangular template pasted on the surface-piercing hydrofoil. Moreover, the MATLAB code can also recognize the transient cavity and spray sheet profiles, such as the maximum cavity length, the diameter of the tip-vortex, and the maximum elevation of the spray sheet. The hydrofoil is piercing the free surface from left to right. The calibration from the image pixel distance to the real distance is varied in the camera shooting window, and thus, we develop and incorporate a dynamic calibration method into the MATLAB code by using different calibration values above and below the free surface to obtain the real distance on each frame.

TABLE I. Foil geometrical dimensions, experimental conditions and the ranges of immersed aspect ratios AR, chord Froude numbers Fr_c, depth Froude number Fr_h, chord Reynolds number Re, and vaporous cavitation number σ.

Chord length	c	0.05 m
Foil span	s	0.25 m
Tip immersed depth	h	0.025, 0.05, and 0.075 m
Yaw angle	α	0°, 5°, 10°, 15°, and 20°
Forward velocities	u	0.36–22.96 m/s
Immersed aspect ratio	$AR = \frac{h}{c}$	0.5, 1.0, and 1.5
Chord Froude number	$Fr_c = \frac{u}{\sqrt{gc}}$	0.51–32.79
Depth Froude number	$Fr_h = \frac{u}{\sqrt{gh}}$	0.51–43.34
Chord Reynolds number	$Re_c = \frac{uc}{\nu}$	1.77×10^4–1.14×10^6
Vaporous cavitation number	$\sigma = \frac{p_{atm} - p_v}{0.5\rho u^2}$	0.37–1517

III. EXPERIMENTAL RESULTS

A. Observations of different flow regimes

In our experiments, the high-speed visualization reveals three distinct flow-regimes under different conditions, namely, Fully Wetted (FW) flows, Fully Ventilated (FV) flows, and Vaporous Cavitating (VC) flows. Figure 4 shows the fully wetted flows at $AR = 1.5$, $\alpha = 0°$, where both the pressure-side and suction-side of the hydrofoil are fully wet without apparent air entrainment along the entire span. This FW flow has also been observed by Harwood *et al.*[4] and Waid.[2] The initially calm water surface is defined as the $z' = 0$ plane by a dashed straight line superimposed on the high-speed images. As shown in Fig. 4(a), the hydrofoil is piercing the free surface from left to right. In the meantime, the sub-atmospheric pressure at the hydrofoil trailing edge generates a downward pressure gradient; it deforms the free surface and entrains air into a base cavity, thereby forming a white foamy wake flow, which is termed as base ventilation. Due to the buoyancy, the bottom of the base cavity continuously rolls up and rises toward the free surface, forming a plunging wave. With the increase in the Froude number, the base cavity becomes longer with striations appearing at the gas–liquid interface due to the Kelvin–Helmholtz instability.

Figure 5 shows another example of a FW flow where an aerated tip-vortex appears below the base ventilation when the hydrofoil has a yaw angle relative to the incoming flow. At a small Froude number, the tip-vortex is too weak to generate the necessary low pressure, so the gas ingested from the base cavity is not sufficient to sustain the

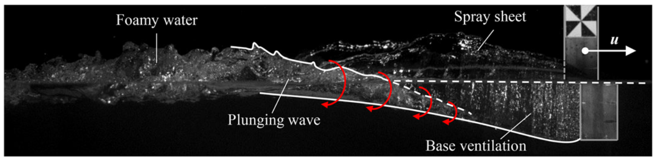

(a)

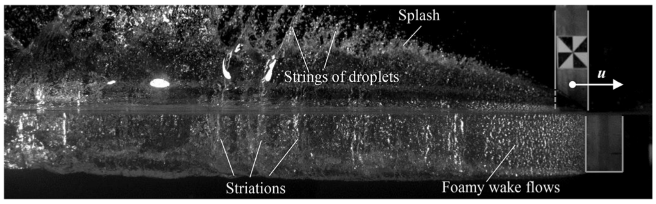

(b)

FIG. 4. High-speed images of fully wetted flows at $AR = 1.5$, $\alpha = 0°$, (a) $Fr_c = 4.66$ and (b) $Fr_c = 13.42$. The base ventilation occurs near the foil trailing edge with a foamy wake. The cavity bottom rolls up toward the free surface due to the buoyancy. With the increase in Froude number, the surface disturbances are more prone to striations.

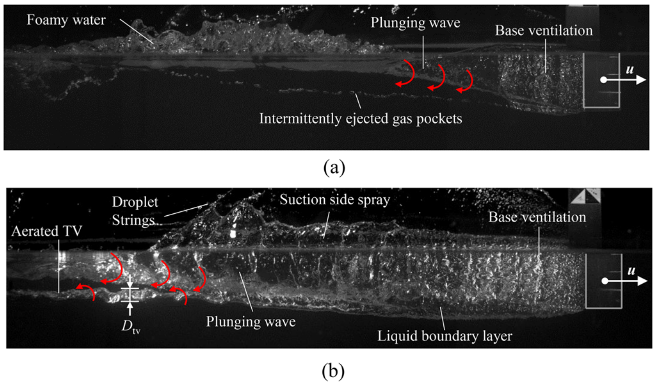

FIG. 5. High-speed images of fully wetted flows with the aerated tip-vortex at $AR = 1.5$, $\alpha = 5°$ (a) $Fr_c = 4.54$, (b) $Fr_c = 9.14$. The aerated tip-vortex rotates in the opposite direction to the plunging wave. A larger Froude number yields a stronger aerated tip-vortex and a longer region affected by the base ventilation. A suction-side spray sheet appears at $\alpha = 5°$.

ventilated tip-vortex and it is ejected intermittently as a gas pocket. Note that the aerated tip-vortex rotates in the opposite direction to the plunging wave. As illustrated in Fig. 5, a larger Froude number yields a stronger aerated tip-vortex and a longer region affected by the base ventilation.

Moreover, the maximum diameter of the tip-vortex (D_{tv}) is extracted from each image, and then, we can find the maximum values in the time series and obtain the non-dimensionalized diameter of the tip-vortex (D_{tv}/c). To further elucidate the effects of different parameters (AR, Fr, α) on the aerated tip-vortex in the FW regime, D_{tv}/c is used to characterize the tip-vortex strength and plotted against the chord Froude number.

As shown in Fig. 6, all experimental points of this state are used to characterize the tip-vortex strength by using D_{tv}/c vs Fr_c. The non-dimensionalized diameter of the tip-vortex (D_{tv}/c) slightly increases with the increase in Fr_c, and it is independent of AR and α in the FW regime.

Figure 7 shows an example of a fully ventilated (FV) cavity, where the initially calm free surface is gashed by the hydrofoil. The suction side of the hydrofoil is entirely enclosed in a ventilated cavity, and the

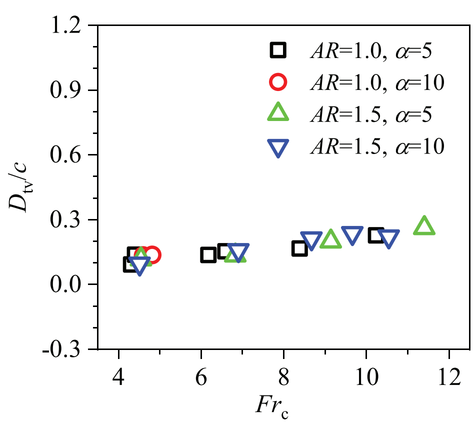

FIG. 6. Non-dimensionalized diameter of the tip-vortex (D_{tv}/c) over a range of chord Froude number (Fr_c) for the FW regime.

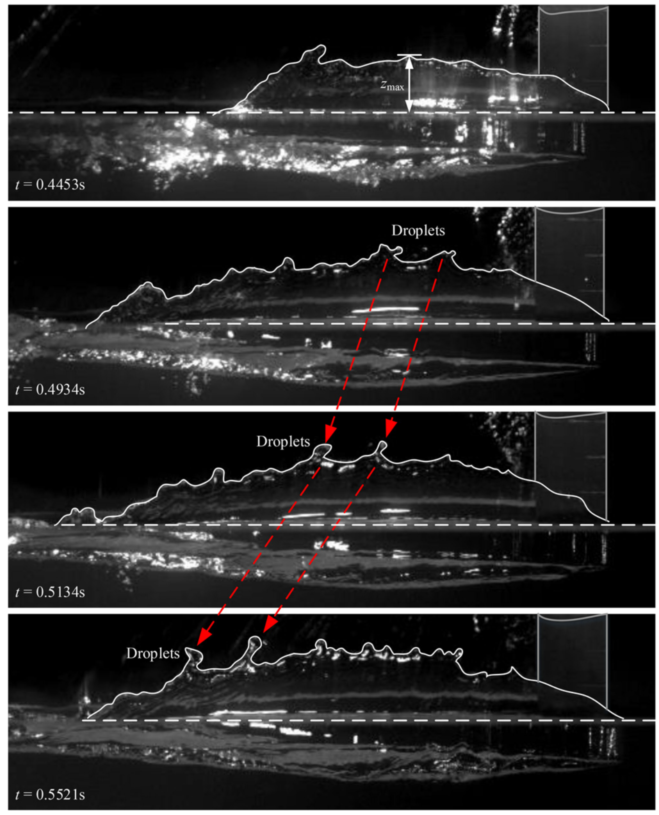

FIG. 7. The evolution of the plunging wave occurring at $AR = 0.5$, $\alpha = 20°$, and $Fr_c = 4.49$. Surface disturbances are observed on the front face of the plunging wave with isolated droplets.

pressure side of the hydrofoil is completely wet, which is also observed by Harwood *et al.*,[4] Breslin and Skalak,[3] although the tests are conducted in different experimental facilities. Flow separates smoothly from the leading edge and tip of the hydrofoil, forming a deformed gas–liquid interface. The angle of the gas–liquid interface to the waterline is very small; therefore, the reentrant jet toward the hydrofoil leading edge does not destabilize the fully ventilated (FV) cavity.[4]

Moreover, the incoming flow impinges against the leading edge of the hydrofoil with forming an upward velocity, and large sprays are generated on both sides of the hydrofoil, which are elevated above the free surface at the leading edge. This is called a bow wave, which has been reported by many researchers.[27–29] The suction-side spray is lower, and its evolution is depicted in Fig. 7. Due to the inertia force, the initial elevated spray ahead of the hydrofoil continues to ride upward until it reaches the maximum height, which is located a certain distance away from the hydrofoil. Meanwhile, the gravity causes the spray sheet to plunge back toward the free surface, forming the plunging wave. Subsequently, the surface tension is not sufficiently strong to persist the stability of the plunging spray, so some isolated droplets flake off from the edge, stretch in length, and propagate downstream as the plunging wave is in free fall, causing the surface disturbances. The surface disturbances are barely visible near the leading edge of the surface-piercing hydrofoil.

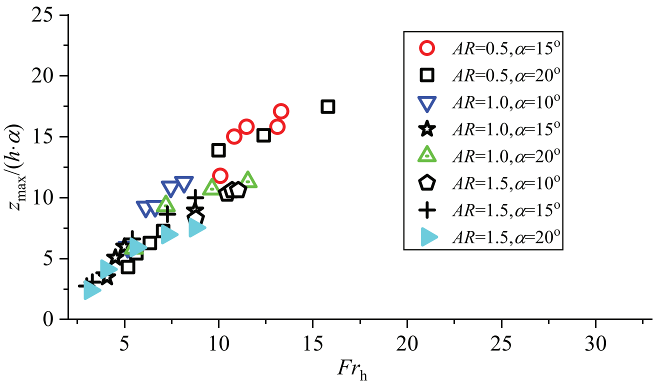

FIG. 8. Non-dimensionalized maximum wave elevation, $Z^* = z_{max}/(hs^2 \cdot \alpha)$, over a range of the depth Froude number (Fr_h).

To further reveal the wave profile, we investigate the variation of the maximum elevation of the suction-side spray above the initial free surface, z_{max}, upon the Froude number. To facilitate the following discussion, a non-dimensionalized maximum wave elevation Z^* is defined as, $Z^* = z_{max}/(h\cdot\alpha)$, where the maximum elevation z_{max} is extracted from the digital images of the wave observed in experiments. For some experimental runs with higher Fr, either the crest of the suction-side wave is out of the camera's field of view, or the wave breaks and splashes very violently, making it impossible for us to accurately grasp the maximum elevation z_{max}, and thus, these runs are not summarized herein.

The non-dimensionalized maximum wave elevation Z^* is plotted over a range of the depth Froude number in the FV regime. As Fig. 8 shows, the yaw angle (α) together with the immersed aspect ratio (AR) does not have a significant effect on the wave elevation, and the Z^* increases upon increasing Fr_h. It is worth noting that when the Fr_h is less than 6, the data points collapse well, but when the Fr_h is greater than 6, the data points are scattered. This may be because the bow wave is linear at low Froude numbers; with the increase in the Froude number, the bow wave exhibits strong nonlinearity characterized by wave breaking and splashing, which is also reflected in the maximum wave elevation, so there is no satisfactory analytical solution to this flow as reported by Waniewski *et al.*[27]

At a very high Froude number and a small yaw angle, the water on the suction surface of the hydrofoil would change from the liquid phase to vaporous phase, appearing as a white cavity, which is called vaporous cavitation. Figure 9 shows the unsteady evolution of the vaporous cavitation at $AR = 1.0$, $\alpha = 5°$, and $Fr_c = 24.46$. A sheet vaporous cavity first starts from the leading edge of the hydrofoil at $t = 0.3155$ s and then gradually develops in the streamwise direction (frame 2–3). During this process, there is no white cavity at the free tip and the free surface, and in contrast, a free-surface seal is observed as a thin layer of sub-cavitating attached flow between the cavity and the free surface, which has also been observed by other scholars.[3,7,8,13] Since the pressure inside the vaporous cavity (that is, $P_v \approx 3$ kPa) is much lower than the atmospheric pressure, a large pressure difference

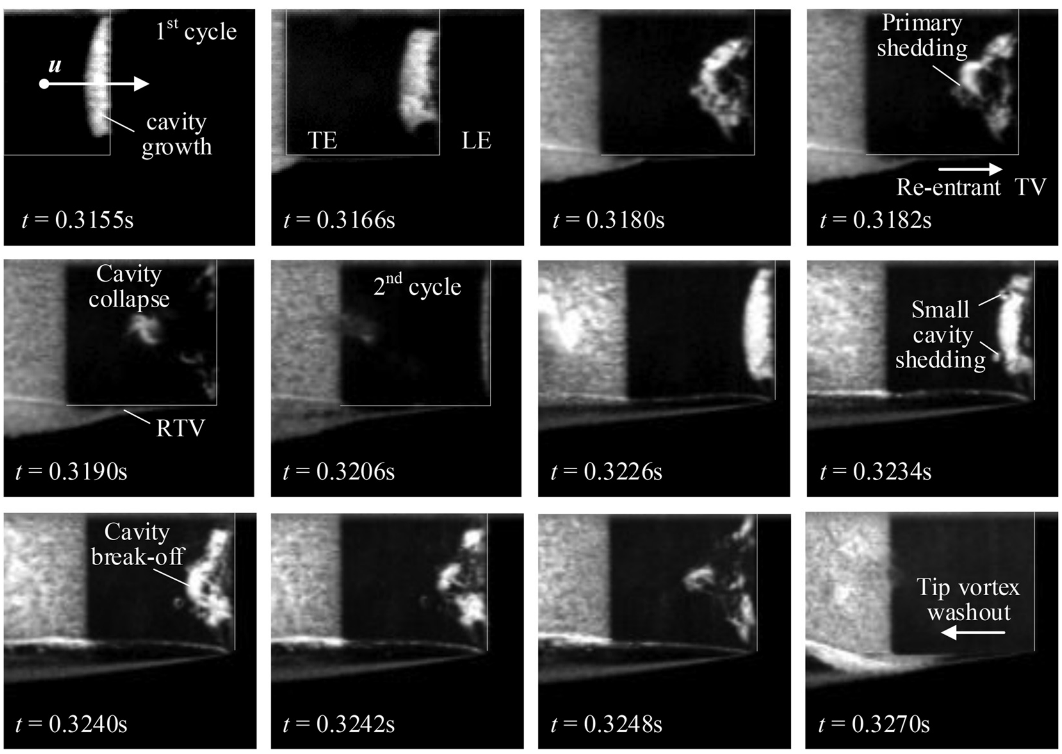

FIG. 9. The unsteady evolution process of the vaporous cavitation at $AR = 1.0$, α=5°, and $Fr_c = 24.46$.

is generated along with the cavity closure, and the cavity is continuously squeezed at the free tip and the free surface, making the cavity closure line more and more convex from $t = 0.3155$ to $t = 0.3180$ s. Subsequently, a primary vapor cloud is shed off at $t = 0.3182$ s, further rolls up, and convects downstream, and finally it collapses at $t = 0.3190$ s. In the meanwhile, an attached cavity begins to grow again at the hydrofoil leading edge at $t = 0.3206$ s and continues to develop in the streamwise direction. It is noted that secondary shedding lobes appear at the sheet cavity at $t = 0.3234$ s. At present, the cavity becomes highly unstable with primary vapor clouds subjecting to the same evolution routine, that is, shedding-off, convecting downstream, and collapsing (frame 9–12).

During this unsteady evolution process, the gas continuously is ingested along with the vortex core from the base cavity, forming a visible white aerated tip-vortex, which moves upstream along the hydrofoil tip and reaches the corner between the hydrofoil tip and the leading edge (frame 1–6). There is a tremendous upward pressure difference between the vaporous cavity and the atmospheric tip-vortex, so the aerated tip-vortex starts to roll up toward the suction surface at $t = 0.3226$ s, gradually expands and then decreases together with the cavity length. Finally, when the cavitation disappears at $t = 0.3270$ s, the aerated tip-vortex is washed downstream by the main flow.

B. Flow-regime transition

In our experiments, the flow-regime transition from FW to FV is achieved through the self-initiated inherent characteristics of the flow, and two ventilation formation mechanisms are observed, i.e., tip-vortex-induced ventilation (TVV) and vapor-cavitation-induced ventilation (VCV). Figures 10 and 11 are two examples of ventilation formation induced by vaporous cavitation.

As shown in Fig. 10, the hydrofoil pierces the free surface at $AR = 0.5$, $\alpha = 10°$, and $Fr_c = 24.65$. A cavity grows from the leading edge at $t = 0.5096$ s and develops in the streamwise direction. Subsequently, the rear of the sheet cavity becomes destabilized and sheds off some pocket vaporous fragments at $t = 0.5148$ s. After that, a large cloud vapor is broken from the attached cavity at $t = 0.5154$ s, and thus, the residual cavity changes from a smooth sheet into a highly

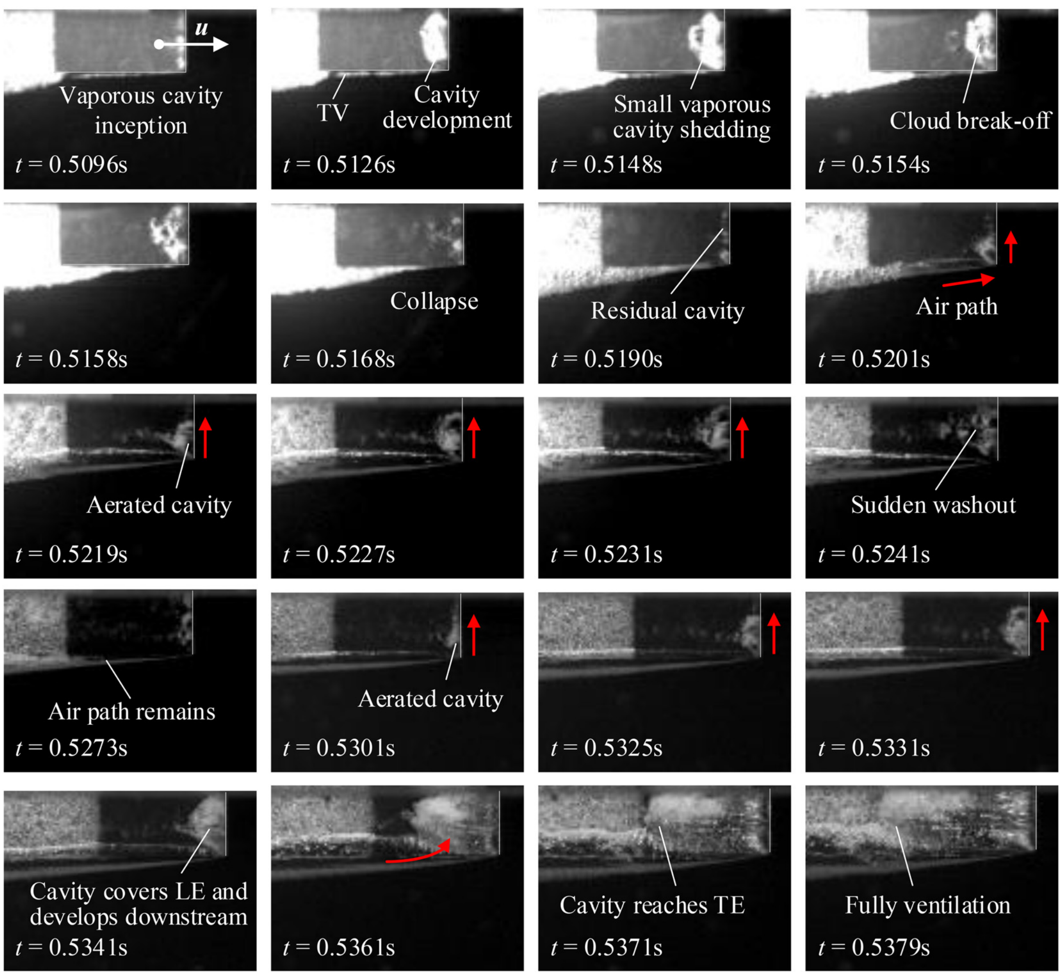

FIG. 10. The unsteady evolution process of the vaporous cavitation and the vapor-cavitation-induced formation occurring at $AR = 0.5$, $\alpha = 10°$, and $Fr_c = 24.65$.

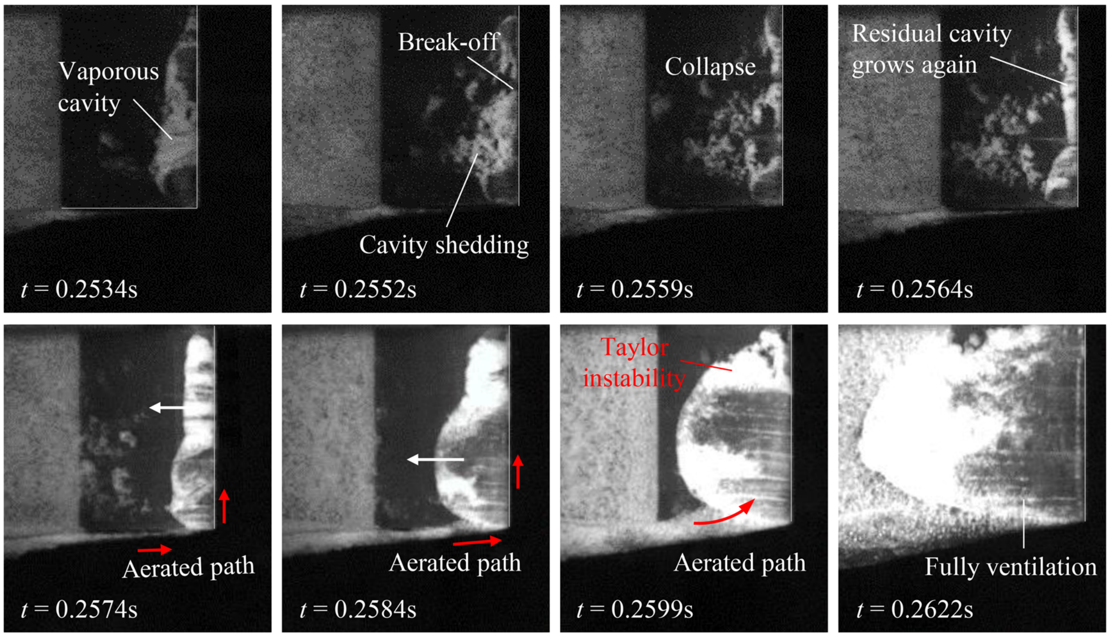

FIG. 11. The unsteady evolution process of the vaporous cavitation and the vapor-cavitation-induced formation occurring at $AR = 1.5$, $\alpha = 5°$, and $Fr_c = 30.09$.

turbulent cloud, which is gradually entrained downstream by the main flow and collapses, leaving a little bit at the leading edge at about $t = 0.5190$ s. During the unsteady evolution process of the vaporous cavity (frame 1–7), the gas in the base-ventilated wake aft of the hydrofoil coalesces in the low-pressure vortex core, causing the tip-vortex to aerate at about $t = 0.5096$ s, and then the aerated vortex core gradually travels upstream until the corner between the hydrofoil tip and the leading edge at about $t = 0.5190$ s. Subsequently, the ventilated tip-vortex expands rapidly, which provides gas to invade toward the free surface, appearing with a continuously enlarged cavity at the hydrofoil leading edge. However, that ventilated bubbly cavity cannot gather and it is washed downstream by the main flow at $t = 0.5241$ s, causing some foamy leftovers scattering on the foil leading edge. Fortunately, the aerated tip-vortex still remains at $t = 0.5273$ s, expands again, and injects gas, forming an aerated cavity near the tip. It is observed to continuously move upward during $t = 0.5301$–0.5331 s, followed by an intersection with the free surface $t = 0.5341$ s. Subsequently, the aerated cavity gradually develops downstream, and meanwhile, the tip-vortex dramatically rolls up at about $t = 0.5361$ s. Their combination would further promote the ventilation formation, and finally, the ventilated cavity reaches the foil trailing edge, resulting in the FV state at about $t = 0.5379$ s.

Figure 11 shows another example of the vapor-cavitation-induced formation. The surface-piercing condition is $AR = 1.5$, $\alpha = 5°$, and $Fr_c = 30.09$. A sheet cavity is attached to the hydrofoil suction-side at about $t = 0.2534$ s and the cavity length gradually increases from the free surface to the hydrofoil tip since the local cavitation number decreases linearly downward. It is worth noting that a pure transparent region appears near the hydrofoil tip (frame 1), which is caused by the huge pressure difference driving the gas into the low-pressure vaporous cavity. There is a white foamy cavity in the middle of the hydrofoil span (frame 1). It becomes unstable immediately and sheds off a large number of small vapor fragments (frame 2), which is caused by the re-entrant flow beneath the vaporous cavity. This shedding of cloud cavities is also observed by Rothblum *et al.*[8] in the wake of a partial vaporous cavity on a surface-piercing strut. Subsequently, those shed vapor fragments are entrained downstream by the main flow and eventually collapse, and only a small amount of vaporous cavities remain attached to the leading edge of the hydrofoil (frame 3). The residual cavity grows again and develops downstream (frame 4–5). Meanwhile, since the air path remains available that pure gas region always exits at the hydrofoil tip (frame 1–4) and continues to expand upward and downstream (frame 5–7) with a convex shape of the cavity closure line, replacing the original white vaporous cavity at the midspan of the foil leading edge. Finally, a fully ventilated flow is achieved at about $t = 0.2622$ s. This is consistent with descriptions in Fig. 10. However, it is particularly important to note that the upper part (adjacent to the free surface) of the ventilated cavity exhibits the Taylor instabilities[30] since it is subject to a dramatic downward acceleration induced by the low cavity pressure.

Tip-vortex-induced ventilation (TVV) is a primary formation mechanism, which has also been observed by other scholars.[3,7,14] Figure 12 shows the tip-vortex-induced ventilation formation, which is broken down into three sequential stages. The flow begins in a FW regime at about $t = 0.0313$ s. A downward pressure gradient drives the air to intrude continuously into the low-pressure region at the hydrofoil trailing edge, forming the base ventilation and making the free surface deformed (as shown in frames 1–4). Subsequently, the air in the base-vented cavity enters the low-pressure core of the tip-vortex and coalesces into an aerated vortex core at $t = 0.1103$ s (frame 5). The white aerated vortex continues to travel along with the low-pressure core toward the hydrofoil leading edge until it reaches the corner

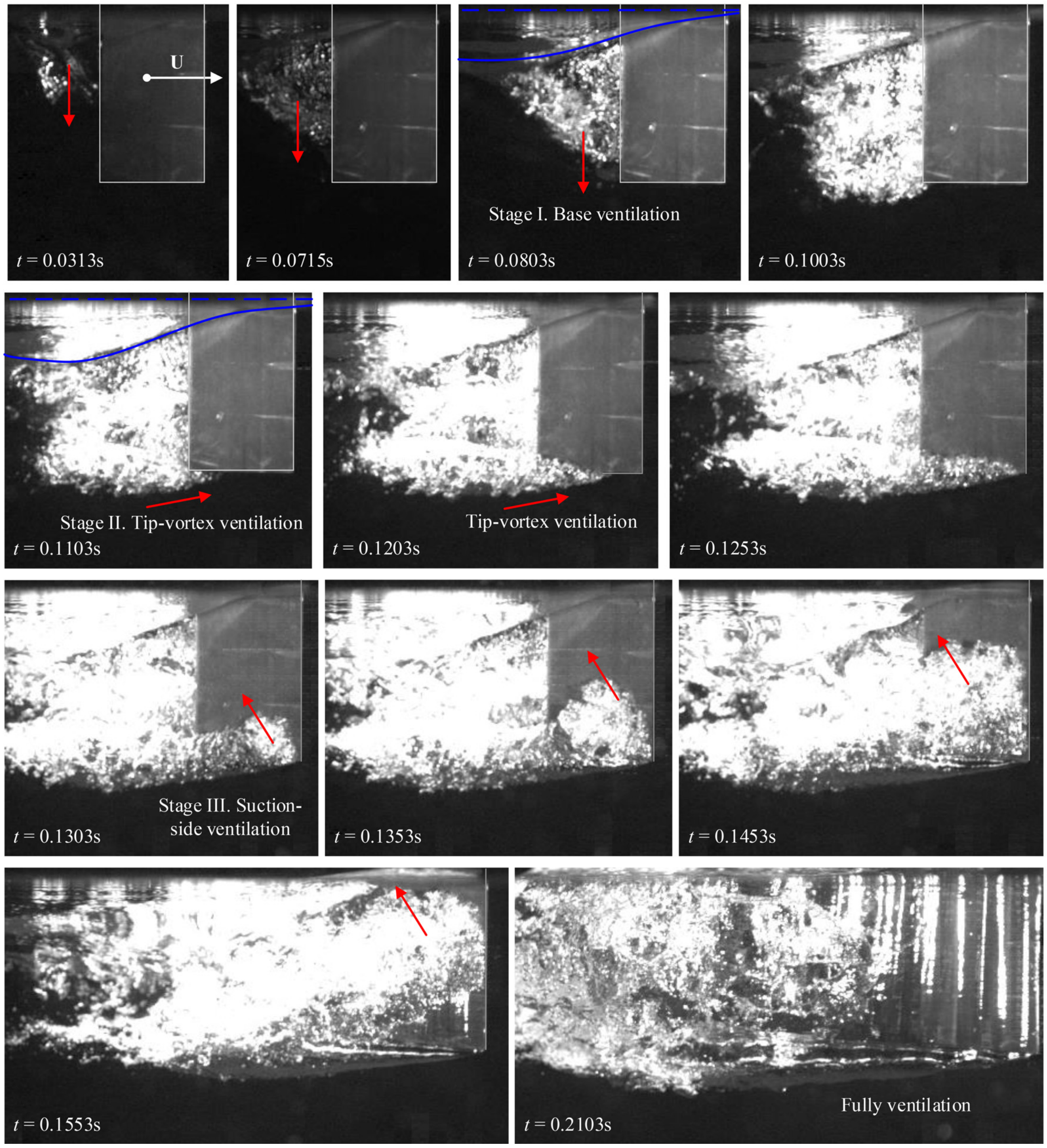

FIG. 12. Tip-vortex-induced ventilation formation occurring at $AR = 1.5$, $\alpha = 20°$, and $Fr_c = 5.24$, which includes three stages, i.e., base ventilation, tip-vortex ventilation, and suction-side ventilation. Red arrows indicate gas-ingress paths.

between the hydrofoil tip and its leading edge at $t = 0.1253$ s (frame 7). When present conditions are sufficient to maintain the sub-atmospheric pressure at the hydrofoil suction-side (a ventilation-prone region), the aerated cavity would expand rapidly both upward the free surface and toward the trailing edge of the hydrofoil during $t = 0.1303$–0.1553 s. This is termed as suction-side ventilation (stage III), showing an oblique upward trajectory from the relative perspective of the surface-piercing hydrofoil. A fully ventilated cavity is finally obtained at $t = 0.2103$ s.

Moreover, we investigate the TVV formation time upon various parameters. It is observed that the formation time at stage II is very short, which has also been established in the literature,[3,4] so the formation time here refers to the time spent in stage III. A non-dimensionalized time, $t^* = t \cdot (c/g)^{-0.5}$, is introduced to characterize the formation time, and it is plotted over a range of the depth Froude number (Fr_h) as shown in Fig. 13. A low-order rational polynomial is fitted with a dashed line by using the experimental data, indicating that the formation time (t^*) is inversely proportional to the Fr_h. As the Fr_h increases, it takes less time

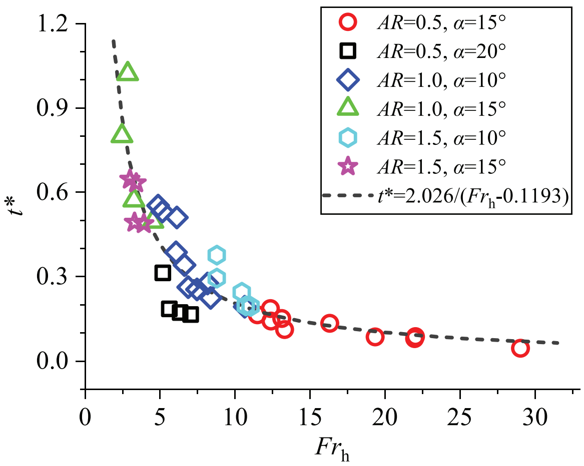

FIG. 13. Non-dimensionalized formation time of the tip-vortex ventilation, $t^* = t \cdot (c/g)^{-0.5}$, as a function of depth Froude number (Fr_h). A low-order rational polynomial is fitted through the experimental data by a dashed line, and the R-square is 0.84 and the RMSE is 0.092.

to complete the suction-side ventilation. Regardless of the yaw angle (α) and the immersed aspect ratio (AR), the formation time (t^*) can be expressed by $t^* = 2.026/(Fr_h - 0.1193)$, but the t^* range is different. For a fixed AR, a larger Fr_h is required for the suction-side ventilation as α decreases, and thus, the required t^* decreases.

C. Flow-regime map

The variations of these flow regimes and the transitions between them are systematically investigated by varying the parameters Fr, α, and AR. The results are summarized in the flow-regime maps (Fr vs α) as shown in Fig. 14. It is worth noting that the flow regimes yield similar trends for different immersed aspect ratios. Specifically, there are three distinct zones (indicated by solid shading) in the parametric maps, including two stable flow-regime zones (i.e., FW zone and FV zone) and one unstable flow-regime zone, which is in good agreement with the notional stability zones of a surface-piercing hydrofoil by Fridsma.[10] For stable zones, the FW state occurs at the lower left of the parametric map, where either Fr_c or α is low. In comparison, the FV state is observed at the top right of the parametric map, where both Fr_c and α range from moderate to high. For $AR = 1.5$, the FW and FV boundaries are vertical at $\alpha \geq 15°$, indicating that it becomes a function of Fr_c only. The unstable zone (indicated by yellow shading) bridges the two stable flow-regime zones. It is either the VC state or the transitional regimes between FW and FV, i.e., tip-vortex-induced ventilation (TVV) and vapor-cavitation-induced ventilation (VCV). At $\alpha > 10°$, TVV is observed with a further increment of Fr_c or α from the FW state. It is worth noting that the VC state is concentrated at a narrow range of high Fr_c with $\alpha \leq 10°$. Upon an increase in Fr_c or α, the flow regime migrates from VC state to VCV and then leads to FV.

Based on the flow-regime maps obtained by our experiments, it has been found that, at high speeds, FW and FV become dominant and two transition processes can support changes from FW to FV, which is following descriptions by Young *et al.*[6] In pursuit of higher speeds, VC flow would inevitably occur and lead to hydrodynamic fluctuations due to the cavitation oscillations; on the other hand, it can promote ventilation formation. In other words, the desired FV state can be achieved not only by increasing α at low-to-moderate Fr_c, but also by the favorable VC flow to enhance the ventilation at moderate-to-high Fr_c. This demonstrates that the stable FV zone can extend to the moderate-to-high Fr range through the vapor-cavitation-induced ventilation, which contributes to the design optimization and control strategies of high-speed hydrofoil vessels.

To illustrate surface-piercing bodies in ventilated cavities, a simple lifting-line model is described in Harwood *et al.*[4,31] Inspired by their work, an improved lifting-line model is further developed by considering the effects of small aspect ratios and free surface to quantitatively elucidate stability boundaries at high speeds in this study.

Based on Prandtl's lifting-line theory, the steady flow past a high-aspect-ratio foil is simplified to one-dimensional spanwise distribution. Faltinsen[32] provided the mathematical expression between the sectional circulation $\Gamma(z')$ and the downwash velocity $w(z')$ in Eq. (1), where z' is the local coordinate position of the submerged part of the hydrofoil to the free surface as shown in Fig. 2(b). Since each integral point (ζ) is not overlapped with the local coordinate position (z'), the integral in Eq. (1) is not singular. The numerical solution of Eq. (1) is described in detail by Harwood,[33]

$$w(z') = \frac{1}{4\pi}\int_0^h \frac{\partial\Gamma(\zeta)}{\partial\zeta}\frac{1}{z'-\zeta}d\zeta. \tag{1}$$

An *induced* angle of attack is produced by the downwash velocity $w(z')$, and it is simplified to $w(z')/u$ at small angles.[34] Although the foil is at a *geometric* angle of attack α_{2D}, the local foil section is seeing a smaller angle, namely, the *effective* angle of attack α_{eff}. Hence, the *geometric* angle of attack (α_{2D}) is a sum of the *effective* angle of attack (α_{eff}) and the dimensionless downwash induced angle (w/u), expressed in the following equation:

$$\frac{w(z')}{u} + \sin\left(\alpha_{eff}(z')\right) = \sin\left(\alpha_{2D}(z')\right). \tag{2}$$

According to the thin-airfoil theory, the lift coefficient in the 2D section $C_{l\text{-}2D}(z')$ is approximately calculated by Eq. (3), where a_0 is the slope of the lift coefficient curve at sub-stall angles. It is noted that Eq. (3) is applicable for the vaporous cavitation observed in our experiments since it occurs at $\alpha \leq 10°$, which is in the sub-stall range,

$$C_{l-2D}(z') = a_0 \sin\left(\alpha_{eff}(z')\right). \tag{3}$$

Subsequently, to consider the effect of the vaporous cavitation on the sectional lift, Tulin[35] gave a linear solution for supercavitation around a flat plate when the dimensionless cavity length is not less than 1.25 (i.e., $l_c/c \geq 1.25$), and Acosta[36] derived a linear solution for partial cavitation where $l_c/c < 0.5$. Both mathematical solutions are pathological at $l_c/c = 1$, but this portion of each solution can be removed as suggested by Brennen,[37] and then l_c/c can be smoothly fitted through the above-mentioned linear solutions by using a rational polynomial in the following equation:

$$\frac{l_c}{c} = \frac{2.67\left(\frac{\sigma}{2\alpha_{eff}}\right) + 96.62}{\left(\frac{\sigma}{2\alpha_{eff}}\right)^3 - 7.1\left(\frac{\sigma}{2\alpha_{eff}}\right)^2 + 49.42\left(\frac{\sigma}{2\alpha_{eff}}\right) + 0.961}. \tag{4}$$

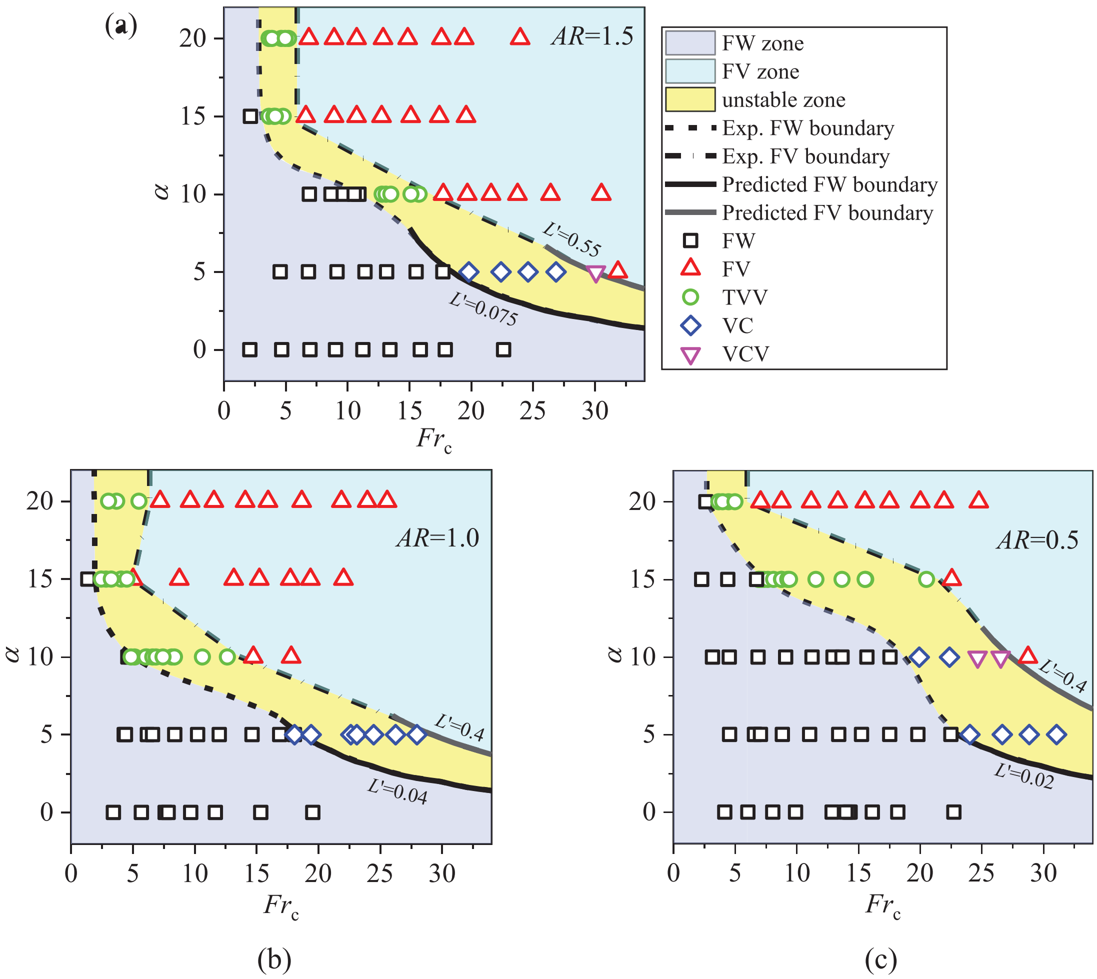

FIG. 14. Flow regime map for an immersed aspect ratio of (a) $AR = 1.5$, (b) $AR = 1.0$, and (c) $AR = 0.5$. Symbols denote five flow patterns: fully wetted flow (FW); fully ventilated flow (FV); tip-vortex-induced ventilation (TVV); vaporous cavitating flow (VC); vapor-cavitation-induced ventilation (VCV). The yellow shaded region indicates experimentally observed unstable flow regimes including TVV, VC, and VCV. The short-dashed line denotes the FW boundary obtained by experiments; the short-dashed-dotted line denotes the FV boundary obtained by experiments. The solid lines are the FW and FV boundaries predicted by the improved lifting-line model.

Herein, σ is cavitation number with the definition in Eq. (5), where p_{atm} is the atmospheric pressure, p_v is the saturated pressure,

$$\sigma = \frac{p_{atm} + \rho g z' - p_v}{0.5\rho u^2}. \tag{5}$$

The slope of the lift coefficient curve is fitted by the following equation:

$$a_0 = \frac{\frac{\pi}{2}\left(\frac{l_c}{c}\right)^3 - 2\left(\frac{l_c}{c}\right)^2 + 4.5\left(\frac{l_c}{c}\right) + 1}{\left(\frac{l_c}{c}\right)^3 - \left(\frac{l_c}{c}\right)^2 + 0.75\left(\frac{l_c}{c}\right) + \frac{1}{2\pi}}. \tag{6}$$

By substituting Eq. (6) into Eq. (3), $C_{l\text{-}2D}(z')$ is obtained, and then the sectional circulation $\Gamma(z')$ is derived from the following equation, where c is the chord length in the 2D section:

$$\Gamma(z') = \frac{1}{2} c \cdot u \cdot C_{l\text{-}2D}(z'). \tag{7}$$

Equations (1)–(7) are primary governing equations for the lifting-line model.[4] An ellipse circulation distribution is used for initialization, and then, a discrete iterative solution is used until the iteration coverages. Finally, the spanwise distribution of the cavity length is obtained. However, the lifting-line model mentioned above is based on the assumption of an infinite aspect ratio, which cannot fully capture present vaporous cavities upon a finite surface-piercing hydrofoil.

In contrast, the improved lifting-line model can consider the effects of small aspect ratios and free surface by embedding a correction to rescale the spanwise distribution of sectional properties. This correction includes two parts in which F_1 is used to correct small aspect-ratios and F_2 is used for the free-surface correction.

F_1 is the scaled-to-unscaled ratio of the 3D lift coefficient due to the small aspect ratios, which is defined in Eq. (8), where C_l^* is the

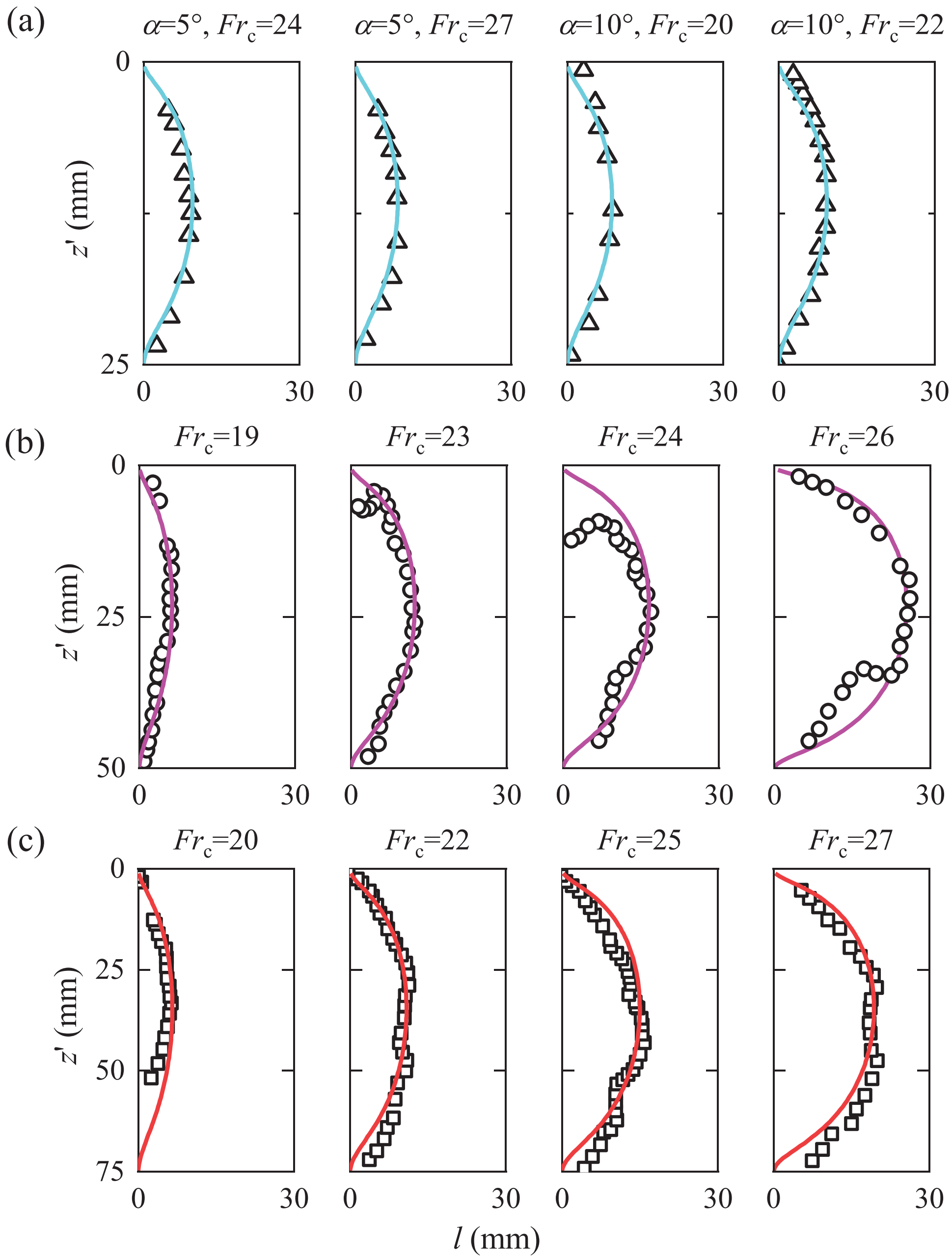

FIG. 15. The spanwise cavity distribution of the surface-piercing hydrofoil (a) $AR = 0.5$, (b) $AR = 1.0$, $\alpha = 5°$, and (c) $AR = 1.5$, $\alpha = 5°$. The solid line represents the cavity profile predicted by the improved lifting-line model, and scattered symbols are extracted from experiments.

unscaled 3D lift coefficient and it is the $C_{l\text{-}2D}$ integral along the span, as expressed in Eq. (9). The Söding's formula[38] in Eq. (10) is adopted to compute the scaled 3D lift coefficient (C_l^T) for straight wings of low aspect-ratios ($AR < 4$), which agrees better with the 3D results than Helmbold's formula does:[34]

$$F_l = \frac{C_l^T}{C_l^*}, \tag{8}$$

$$C_l^* = \frac{1}{h}\int_0^h C_{l-2D}(z')dz', \tag{9}$$

$$C_l^T = \frac{AR(AR+1)}{(AR+2)^2} a_0^* \sin(\alpha_{2D}), \tag{10}$$

where a_0^* is the lift-weighted mean value and defined in the following equation:

$$a_0^* = \frac{1}{hC_l^*}\int_0^h \frac{[C_{l-2D}(z')]^2}{\alpha_{2D}} dz'. \tag{11}$$

The presence of the free surface causes a C_l reduction than for infinite fluid, and its influence is higher for smaller submergences.[32] When

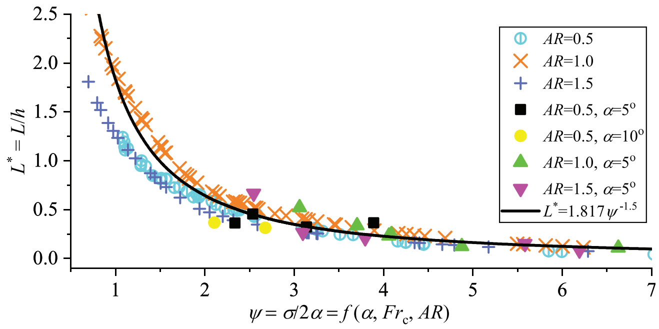

FIG. 16. Non-dimensionalized cavity length ($L^* = L/h$) against the cavitation parameter, $\psi = \sigma/2\alpha = f(\alpha, Fr_c, AR)$. A power function is fitted through the data obtained by both experiments and the improved lifting-line model, with the equation as $L^* = 1.817\psi^{-1.5}$.

$Fr_h > 10/\sqrt{AR}$, C_l is nearly independent of Fr_h and it decreases with the decrease in the immersed aspect ratio,[39] so the free-surface correction gives in the following equation:

$$F_2 = \frac{1 + 16AR^2}{2 + 16AR^2}. \tag{12}$$

Finally, the unscaled $C_{l\text{-}2D}$ in Eq. (7) is replaced by a scaled value ($F_1 F_2 C_{l-2D}$) and then start a new iterative solution.

As shown in Fig. 15, the vaporous cavity spanwise distribution for the surface-piercing hydrofoil is compared between the experiments and the prediction by the improved lifting-line model. It is found that the cavity length first increases to a maximum and then gradually decreases from the hydrofoil tip toward the free surface. The cavity outline is convex as the whole, and it becomes irregular near the hydrofoil tip and free surface. The predicted cavity profiles are reasonably consistent with the experiments, indicating that the improved lifting-line model is capable of capturing qualitative features of the vaporous cavity near a free surface.

Through the iterative solution of the improved lifting-line model, we can obtain the vaporous cavity profiles for any specified parameter combination (α, Fr_c, and AR), which yields a single dimensionless ratio $\psi = \sigma/2\alpha$. The maximum cavity length (L) is nondimensionalized by the tip immersed depth, resulting in a dimensionless cavity length (L^*), i.e., $L^* = L/h$. Both the L^* solutions and experimental values are plotted against ψ in Fig. 16. The dimensionless cavity length (L^*) gradually decreases as the ψ increases. The predicted L^* is in reasonable agreement with the experiments. Both the predicted and experimental results collapse into a curve, which can be fitted by a power function and the equation is $L^* = 1.817\psi^{-1.5}$. Therefore, for a surface-piercing hydrofoil under a given condition (α, Fr_c, and AR), the maximum length of the vaporous cavity can be deduced theoretically as the following equation:

$$L' = L/c = 1.817AR \cdot \left(\frac{1}{\alpha {Fr_c}^2}\left(\frac{p_\infty - p_v}{\rho g c} + \frac{AR}{2}\right)\right)^{-1.5}. \tag{13}$$

Thus, the inception boundary of the vaporous cavity (i.e., FW boundary) is assumed that the maximum cavity length (L'=L/c) is close to zero, and the criterion of the vaporous cavity to lose its stability (i.e., FV boundary) becomes that $L' = 0.4$ for $AR = 0.5$–1.0 and $L' = 0.55$ for $AR = 1.5$, as shown in Fig. 14. Although the improved lifting-line model is not high fidelity, it yields surprisingly good predictions of the FW and FV boundaries when compared with the experiments. The remarkable thing is that the instability boundary of vaporous cavitation is smaller than that in a water tunnel (generally, L' is about 0.7),[40] and this may be because the presence of the free surface is more likely to promote any disturbance and leads to ventilation.

IV. CONCLUSIONS

In this work, we systematically investigate the ventilated cavities for a surface-piercing hydrofoil in a constrained-launching tank at the Institute of Mechanics, Chinese Academy of Sciences. The experiments are conducted under atmospheric pressure over a wide range of Froude number (Fr), immersed aspect ratio (AR), and yaw angle (α). Three distinct flow regimes are observed using high-speed photography, including the flow wetted flow (FW), fully ventilated flow (FV), and vaporous cavitating flow (VC). FW flows occur when either Fr or α is low, and two lateral sides of the hydrofoil are fully wet except for the base ventilation near the foil trailing edge. In contrast, FV flows occur at moderate-to-high Fr and α, the suction side of the hydrofoil is entirely enclosed in a ventilated cavity and the pressure side of the hydrofoil is fully wet. Interestingly, at high Fr with $\alpha \leq 10°$, vaporous cavitation appears on the suction side of the surface-piercing hydrofoil, and this is an unsteady evolution process with about 3–4 cycles, which is accompanied by the cavity inception, growth, shedding-off, and collapse.

These flow regimes are summarized in flow-regime maps (Fr vs α), which yield similar trends for different immersed aspect ratios. FW and FV are stable flow regimes. The transition from FW to FV is stimulated by two mechanisms, that is, the tip-vortex-induced ventilation (TVV) and vapor-cavitation-induced ventilation (VCV). TVV primarily occurs at $\alpha \geq 10°$ when either Fr or α is further increased starting at the FW state. In the TVV process, the air would coalesce in the low-pressure vortex core, and thus, the tip-vortex is aerated and continually travels upstream along the low-pressure path at the foil tip. When the sub-atmospheric pressure can be maintained at the hydrofoil

TABLE II. Effects of the Re_c by changing the fluid viscosity at $AR = 1.0$, $\alpha = 12.5°$. The kinematic viscosity of the experimental fluid is $\nu_0 = 1.01 \times 10^{-6}$ m²/s, and the chord length of the plate hydrofoil model is $c_0 = 0.05$ m.

Fr_c	ν/ν_0	c/c_0	Re_c	State
11.29	2	1	1.96×10^5	FW → FV
	1		3.91×10^5	FW → FV
	0.5		7.82×10^5	FW → FV
	0.25		1.56×10^6	FW → FV
5.0	2	1	8.66×10^4	FW → FV
	1		1.73×10^5	FW → FV
	0.5		3.47×10^5	FW → FV
	0.25		6.93×10^5	FW → FV
2.15	2	1	3.71×10^4	FW
	1		7.43×10^4	FW
	0.5		1.49×10^5	FW
	0.25		2.97×10^5	FW

TABLE III. Effects of the Re_c by changing the chord length at $AR = 1.0$, $\alpha = 12.5°$. The kinematic viscosity of the experimental fluid is $\nu_0 = 1.01 \times 10^{-6}$ m^2/s, and the chord length of the plate hydrofoil model is $c_0 = 0.05$ m.

Fr_c	ν/ν_0	c/c_0	Re_c	State
		1	3.91×10^5	FW → FV
11.29	1	2	7.82×10^5	FW → FV
		4	1.56×10^6	FW → FV
		1	1.73×10^5	FW → FV
5.0	1	2	3.47×10^5	FW → FV
		4	6.93×10^5	FW → FV
		1	7.43×10^4	FW
2.15	1	2	1.49×10^5	FW
		4	2.97×10^5	FW

suction side, the aerated tip-vortex will rapidly expand upward and downstream until FV is achieved, and the TVV formation time (t^*) is inversely proportional to the Fr_h.

In addition to the well-known TVV, the promotion of the vaporous cavitation to the ventilation formation is revealed in our experiments. It has to meet two things: the air must be able to move upstream along the tip-vortex path and reach the leading edge of the hydrofoil; at that moment, the low-pressure, separated vaporous cavity is still available as a ventilation-prone region to allow the air ingress. Upon an increase in Fr_c or α, the vaporous cavity would eventually be vented to the FV state.

An improved lifting-line model is proposed, which considers the influence of small aspect ratios and free surface by embedding a correction to rescale the spanwise distribution of sectional properties. The predicted cavity profiles are reasonably consistent with the experiments. Both the predicted and experimental results collapse into a curve, indicating that the vaporous cavity length follows a power relation against the cavitation parameter. Therefore, the instability boundary of the vaporous cavity is surprisingly well predicted when compared with the experiments.

ACKNOWLEDGMENTS

The authors would like to acknowledge gratefully the National Natural Science Foundation of China (Nos. 52006232 and 12122214).

AUTHOR DECLARATIONS

Conflict of Interest

The authors have no conflicts to disclose.

DATA AVAILABILITY

The data that support the findings of this study are available from the corresponding author upon reasonable request.

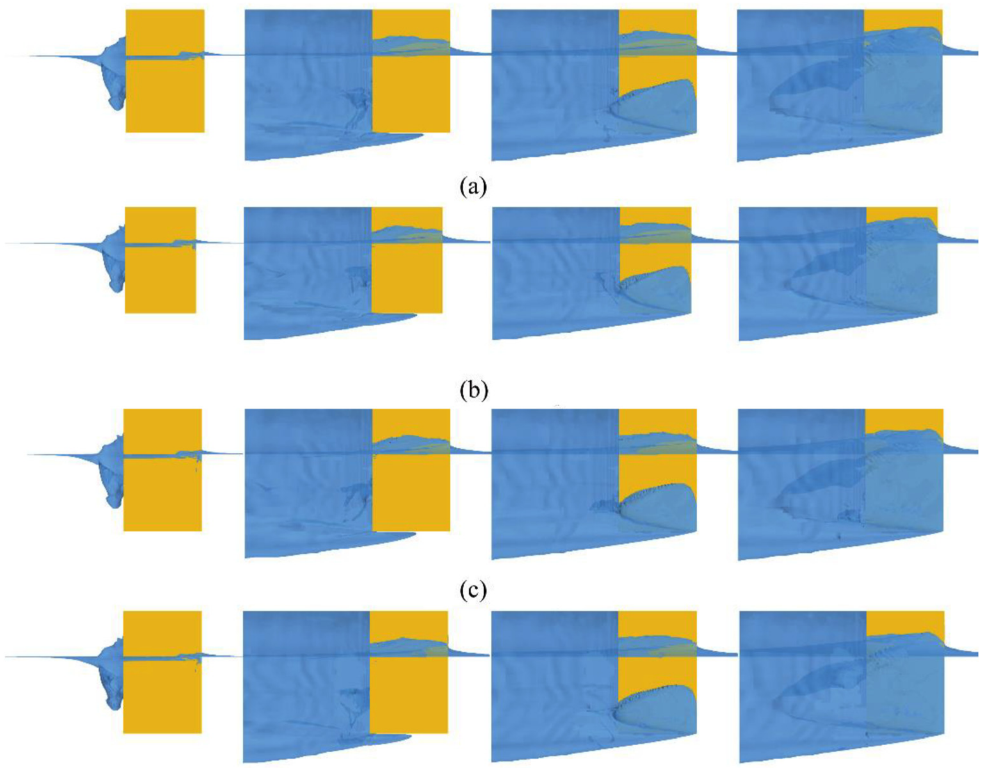

FIG. 17. Dependence of ventilated cavities upon the Re_c by changing the fluid viscosity at $AR = 1.0$, $\alpha = 12.5°$, $Fr_c = 11.29$. (a) $\nu = 2.00\nu_0$, (b) $\nu = 1.00\nu_0$, (c) $\nu = 0.50\nu_0$, and (d) $\nu = 0.25\nu_0$.

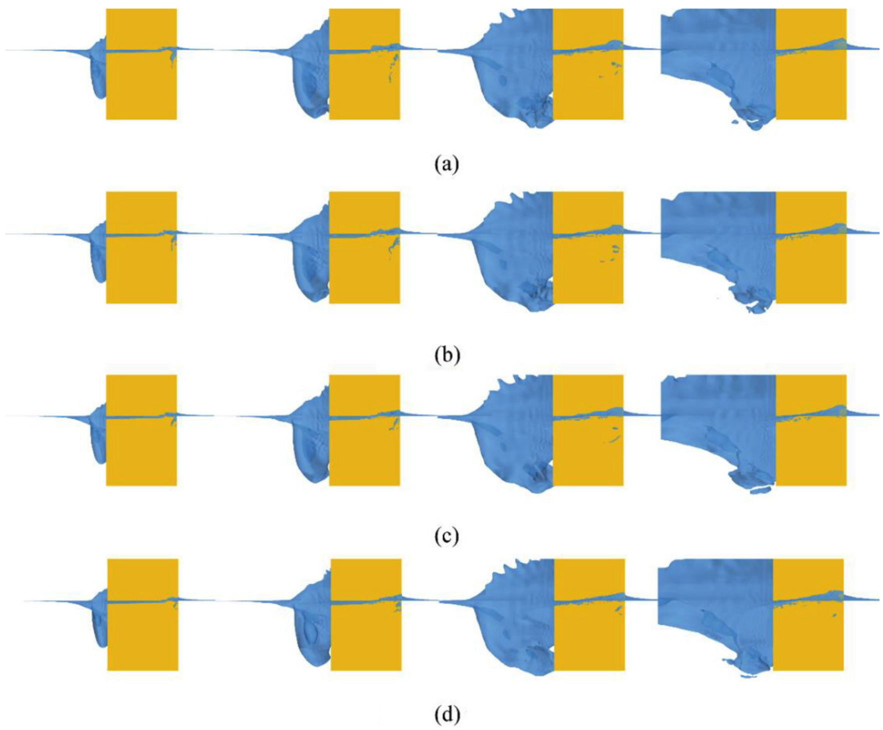

FIG. 18. Dependence of ventilated cavities upon the Re_c by changing the fluid viscosity at $AR = 1.0$, $\alpha = 12.5°$, $Fr_c = 2.15$. (a) $\nu = 2.00\nu_0$, (b) $\nu = 1.00\nu_0$, (c) $\nu = 0.50\nu_0$, and (d) $\nu = 0.25\nu_0$.

APPENDIX: EFFECTS OF REYNOLDS NUMBERS

Dependence of the ventilated cavities on the Reynolds number is studied with the Froude number fixed. The Reynolds number is adjusted by (i) changing the fluid viscosity and (ii) increasing the chord length of the plate hydrofoil. Three Froude numbers are selected from Fig. 14(b) with $AR = 1.0$, $\alpha = 12.5°$. In our experiments, the flow at $Fr_c = 2.15$ is fully wetted, and the flow at $Fr_c = 5.0$ and $Fr_c = 11.29$ is unstable that the FW state would transit to the FV state.

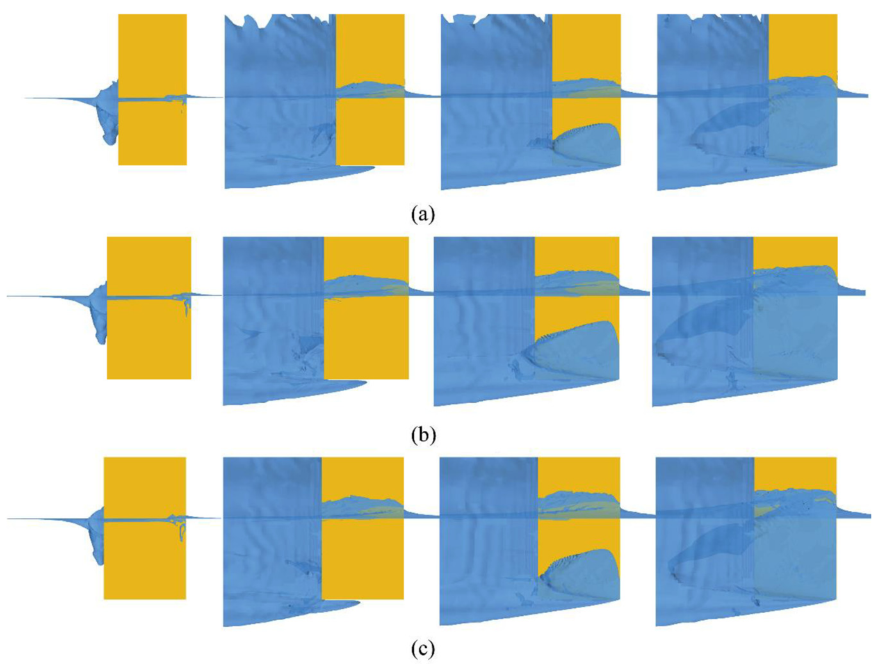

FIG. 19. Dependence of ventilated cavities upon the Re_c by changing the chord length at $AR = 1.0$, $\alpha = 12.5°$, $Fr_c = 11.29$. (a) $c = 1.00c_0$, (b) $c = 2.00c_0$, and (c) $c = 4.00c_0$.

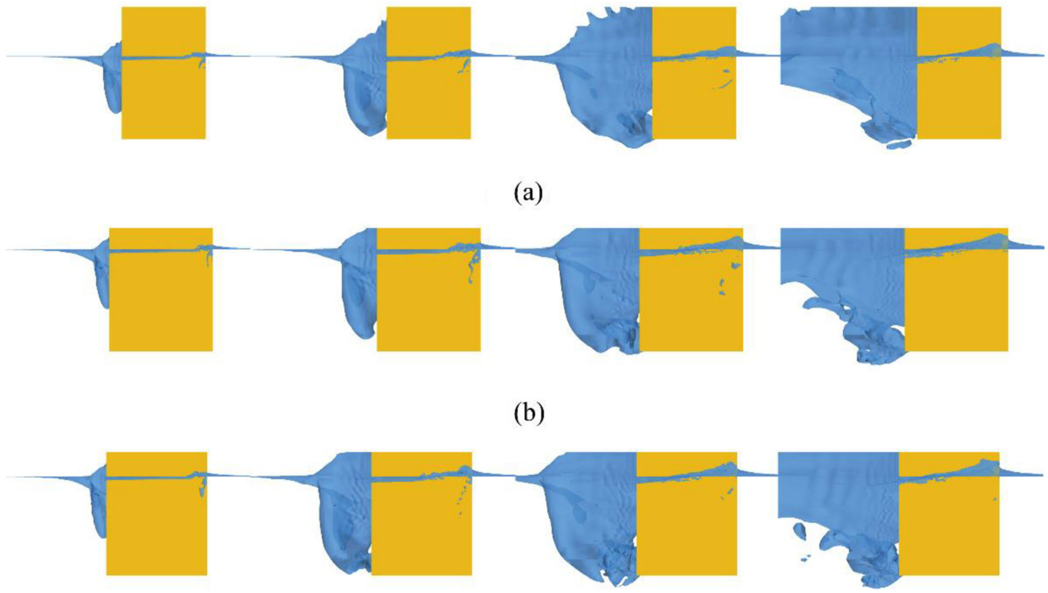

FIG. 20. Dependence of ventilated cavities upon the Re_c by changing the chord length at $AR = 1.0$, $\alpha = 12.5°$, $Fr_c = 2.15$. (a) $c = 1.00c_0$, (b) $c = 2.00c_0$, and (c) $c = 4.00c_0$.

Numerical simulations are adopted to investigate the effects of Reynolds number by using the unsteady Reynolds-averaged Navier–Stokes (RANS) method together with a Volume of Fluid (VOF) model. Present numerical approach has been described in detail in our previous work,[24] and it is proved to be able to accurately capture the unsteady ventilated cavities when compared with the experiments.[4]

The simulated conditions are listed in Tables II and III with the transient flow patterns shown in Figs. 17–20. No matter whether the Re_c is changed by varying the viscosity or the chord length, it can be found that the Re_c does not change the flow regime together with the ventilation formation mechanism. Take the case of $AR = 1.0$, $\alpha = 12.5°$, and $Fr_c = 11.29$ in Table II for example, the Re_c increases from 1.96×10^5 to 1.56×10^6 by decreasing the fluid viscosity from $\nu = 2.0\nu_0$ to $\nu = 0.25\nu_0$, but the evolution of the flow regime remains unchanged. Specifically, the flow begins in a FW regime, then the transition from FW to FV is stimulated by the tip-vortex ventilation mechanism, and finally, fully ventilation is achieved as shown in Fig. 17. The numerical results demonstrate that the ventilated cavities around a surface-piercing hydrofoil are not sensitive to the variation of Reynolds number.

In contrast, the flow regime changes significantly with the Froude number. Take Fig. 17 and Fig. 18 for comparison, it eventually becomes a fully ventilated state at $Fr_c = 11.29$, whereas the flow is fully wetted at $Fr_c = 2.15$, regardless of the Reynolds number. In addition, the variation of flow pattern is also applicable to the case where the Re_c is changed by the chord lengths. Based on the numerical simulations, the dominant parameter in the ventilated cavities is the Froude number rather than the Reynolds number. That is why the flow regime map is plotted with Fr instead of the speed.

REFERENCES

1. B. Perry, "Experiments on struts piercing the water surface," Technical Report No. E-55. 1 (California Institute of Technology, Pasadena, CA, 1954).
2. R. L. Waid, "Experimental investigation of the ventilation of vertical surface-piercing struts in the presence of cavitation," Technical Report No. AD0738493 (Naval Ship Research and Development Center, Sunnyvale, CA, 1968).
3. J. P. Breslin and R. Skalak, "Exploratory study of ventilated flows about yawed surface-piercing struts," Technical Report No. 2-23-59W (NASA Technical Memorandum, Washington, DC, 1959).
4. C. M. Harwood, Y. L. Young, and S. L. Ceccio, "Ventilated cavities on a surface-piercing hydrofoil at moderate Froude numbers: Cavity formation, elimination and stability," J. Fluid Mech. **800**, 5–56 (2016).
5. R. S. Rothblum, "Investigation of methods of delaying or controlling ventilation on surface piercing struts," Ph.D. thesis (University of Leeds, 1977).
6. Y. L. Young, C. M. Harwood, F. Miguel Montero, J. C. Ward, and S. L. Ceccio, "Ventilation of lifting bodies: Review of the physics and discussion of scaling effects," Appl. Mech. Rev. **69**(1), 010801 (2017).
7. P. D. Swales, A. J. Wright, R. C. McGregor, and R. Rothblum, "The mechanism of ventilation inception on surface piercing foils," J. Mech. Eng. Sci. **16**(1), 18–24 (1974).
8. R. S. Rothblum, D. A. Mayer, and G. M. Wilburn, "Ventilation, cavitation and other characteristics of high speed surface-piercing struts," Technical Report No. 3023 (Naval Ship Research and Development Center, Washington, DC, 1969).
9. T. Kiceniuk, "A preliminary experimental study of vertical hydrofoils of low aspect ratio piercing a water surface," Technical Report No. E-55. 2 (California Institute of Technology, Pasadena, CA, 1954).
10. G. Fridsma, "Ventilation inception on a surface-piercing dihedral hydrofoil with plane-face wedge section," Technical Report No. 952 (Stevens Institute of Technology, Hoboken, NJ, 1963).
11. K. I. Matveev, M. P. Wheeler, and T. Xing, "Numerical simulation of air ventilation and its suppression on inclined surface-piercing hydrofoils," Ocean Eng. **175**, 251–261 (2019).

[12]J. Wetzel, "Experimental studies of air ventilation of vertical semi-submerged bodies," Technical Report No. 57 (University of Minnesota, Minneapolis, MN, 1957).
[13]K. L. Wadlin, "Mechanics of ventilation inception," in *Second Symposium on Naval Hydrodynamics* (U.S. Office of Naval Research, 1958), pp. 425–446.
[14]J. A. Ramsen, "An experimental hydrodynamic investigation of the inception of vortex ventilation," Technical Report No. 3903 (National Advisory Committee for Aeronautics, Washington, DC, 1957).
[15]R. C. Mcgregor, A. Wright, P. Swales, and G. Crapper, "An examination of the influence of waves on the ventilation of surface-piercing struts," J. Fluid Mech. **61**(1), 85–96 (1973).
[16]J. C. Ward, C. M. Harwood, and Y. L. Young, "Inverse method for hydrodynamic load reconstruction on a flexible surface-piercing hydrofoil in multi-phase flow," J. Fluids Struct. **77**, 58–79 (2018).
[17]B. Ji, X. Luo, R. E. A. Arndt, and Y. Wu, "Numerical simulation of three dimensional cavitation shedding dynamics with special emphasis on cavitation–vortex interaction," Ocean Eng. **87**, 64–77 (2014).
[18]B. Ji, X. Luo, Y. Wu, X. Peng, and Y. Duan, "Numerical analysis of unsteady cavitating turbulent flow and shedding horse-shoe vortex structure around a twisted hydrofoil," Int. J. Multiphase Flow **51**, 33–43 (2013).
[19]J. C. W. Coffee and R. E. McKann, "Hydrodynamic drag of 12- and 21-percent-thick surface-piercing struts," Technical Report No. 3093 (NACA Technical Note, Washington, DC, 1953).
[20]G. I. Taylor, "The instability of liquid surfaces when accelerated in a direction perpendicular to their planes. I," Proc. R. Soc. London, Ser. A **201**(1065), 192–196 (1950).
[21]Z. Li, C. Liu, D. Wan, and C. Hu, "High-fidelity simulation of a hydraulic jump around a surface-piercing hydrofoil," Phys. Fluids **33**(12), 123304 (2021).
[22]Y. Hu, C. Liu, C. Hu, and D. Wan, "Numerical investigation of flow structure and air entrainment of breaking bow wave generated by a rectangular plate," Phys. Fluids **33**(12), 122113 (2021).
[23]Z. Wang, H. Cheng, and B. Ji, "Euler–Lagrange study of cavitating turbulent flow around a hydrofoil," Phys. Fluids **33**(11), 112108 (2021).
[24]Y. Zhi, J. Zhan, R. Huang, R. Qiu, and Y. Wang, "Numerical investigations into the ventilation elimination mechanism of a surface-piercing hydrofoil," Ocean Eng. **243**, 110225 (2022).
[25]Y. Wang, C. Huang, T. Du, R. Huang, Y. Zhi, Y. Wang, Z. Xiao, and Z. Bian, "Research on ventilation and supercavitation mechanism of high-speed surface-piercing hydrofoil," Phys. Fluids **34**(2), 023316 (2022).
[26]A. Karn, R. E. A. Arndt, and J. Hong, "An experimental investigation into supercavity closure mechanisms," J. Fluid Mech. **789**, 259–284 (2016).
[27]T. A. Waniewski, C. E. Brennen, and F. Raichlen, "Bow wave dynamics," J. Ship Res. **46**(1), 1–15 (2002).
[28]H. Miyata and T. Inui, "Nonlinear ship waves," Adv. Appl. Mech. **24**, 215–288 (1984).
[29]R. R. Dong, J. Katz, and T. T. Huang, "On the structure of bow waves on a ship model," J. Fluid Mech. **346**, 77–115 (1997).
[30]D. J. Lewis, "The instability of liquid surfaces when accelerated in a direction perpendicular to their planes. II," Proc. R. Soc. London, Ser. A **202**(1068), 81–96 (1950).
[31]C. Harwood and Y. Young, "A physics-based gap-flow model for potential flow solvers," Ocean Eng. **88**, 578–587 (2014).
[32]O. M. Faltinsen, *Hydrodynamics of High-Speed Marine Vehicles* (Cambridge University Press, 2005).
[33]C. M. Harwood, "The hydrodynamic and hydroelastic responses of rigid and flexible surface-piercing hydrofoils in multi-phase flows," Ph.D. thesis (The University of Michigan, 2016).
[34]J. D. Anderson, Jr., *Fundamentals of Aerodynamics*, 5th ed. (McGraw-Hill Education, 2010).
[35]M. P. Tulin, "Steady two-dimensional cavity flows about slender bodies," Technical Report No. 834 (United States Navy Department-David W. Taylor Model Basin, Bethesda, MA, 1953).
[36]A. J. Acosta, "Note on partial cavitation of flat plate hydrofoils," Technical Report No. E-19.9 (California Institute of Technology, Pasadena, CA, 1955).
[37]C. E. Brennen, *Cavitation and Bubble Dynamics* (Cambridge University Press, 1995).
[38]H. Söding, "Prediction of ship steering capabilities," Schiffstechnik **29**(1), 3–29 (1982).
[39]G. R. Hough and J. P. Moran, "Froude number effects on two-dimensional hydrofoils," J. Ship Res. **13**(1), 53–60 (1969).
[40]B. Huang, A. Ducoin, and Y. L. Young, "Physical and numerical investigation of cavitating flows around a pitching hydrofoil," Phys. Fluids **25**(10), 102109 (2013).